

Tribocorrosion behaviour of $TiB_xC_y/a-C$ nanocomposite coating in strong oxidant disinfectant solutions

E. Gracia-Escosa¹, I. García¹, J.C. Sánchez-López², M. D. Abad², A. Mariscal², M. A. Arenas¹, J. de Damborenea¹, A. Conde¹

¹CENIM-CSIC, Surface Engineering, Corrosion and Durability department, Av. Gregorio del Amo 8, E-28040 Madrid, Spain

²Instituto de Ciencia de Materiales de Sevilla, (CSIC-US), Av. Américo Vespucio 49, E-41092 Sevilla, Spain

Abstract

Corrosion and tribocorrosion studies of a $TiB_xC_y/a-C$ coating deposited on AISI 316L steel have been performed in an aqueous solution of 0.26 vol.% acetic, 0.16 vol.% peracetic and 0.18 vol.% hydrogen peroxide (commercial product Oxonia 1 vol. %). The corrosion current density of the $TiB_xC_y/a-C$ coating ranges on the same order as bare steel but with a significantly decreasing friction (0.1 vs. 0.6) and wear rate (~ 10 times lower). The compact microstructure of the coating hinders the access of the aggressive electrolyte to the substrate, preventing the onset of the corrosion attack, while maintaining an excellent tribological behaviour in strong oxidant solutions.

Keywords: Sputtered films; steel; polarization; amorphous structures; acid corrosion; passive films

1. Introduction

Over the past decade, many research efforts have focused on the development of multicomponent and multifunctional coatings based on a nanocomposite design, with the purpose of increasing material's performance under severe corrosion, oxidation, and working conditions [1-3]. Nanocomposite hard coatings are typically formed by the combination of at least two immiscible phases, typically consisting of nanocrystalline

transition metal carbides, borides or nitrides and an amorphous phase. The nanocomposites including amorphous carbon (a-C) as secondary phase are promising materials as protective coatings due to their appropriate combination of hardness along with additional interesting properties which are applicable to engineering applications such as low friction coefficient, wear resistance and toughness. In this line, $TiB_xC_y/a-C$ nanocomposite coatings have shown a high degree of hardness, excellent wear resistance and low friction values under non-lubricated conditions [4-7]. For instance, in dry sliding tests performed against 100Cr6 steel and WC balls, a $TiB_xC_y/a-C$ nanocomposite coating showed lower friction coefficient (0.2) than the TiB_xC_y compound without a-C phase in its structure (0.8) [5]. From corrosion viewpoint, the requirements for effective protection include chemical inertness, high electrical resistance together with microstructural demands (high density, low microporosities and diffusion pathways, and good adhesion). Of the different candidates, Diamond-like carbon (DLC) is probably the most studied tribological coating for wear resistant applications such as cutting tools, automotive components and orthopaedic prostheses [8-12]. Due to their excellent biocompatibility and wear properties, DLCs, as single, doped, multiple or gradient layers can increase the corrosion resistance of metals used in a body fluid environment [9, 10]. Conversely, very few papers have evaluated the corrosion resistance of nanocomposite carbon-based coatings [13-15]. Gorokhovskiy et al. evaluated the corrosion resistance of multilayer nanocomposite TiCrCN/TiCr+TiBC cermet coatings developed for advanced tribological applications by means of salt-fog tests. These coatings are very complex, although described in a very simple way they consist of two segments such as TiCrCN+TiBC. The authors concluded that the TiCrCN segment provides corrosion resistance and elastic support for the TiBC segment, which provides wear resistance. Salt spray tests confirmed that the thickness of the TiCrCN segment plays a key role on the corrosion resistance although coupons tested with the TiBC top segment also showed improved corrosion resistance, with the best performance exhibited by the TiBC in multilayer configuration (ML) [13].

Conversely, the corrosion resistance for titanium-based ceramic layers such as TiB_2 , TiN, TiC or TiBN has been widely studied and compared in acid and neutral media [16-22]. Different results have been reported depending on the media employed, as, for instance, TiB_2 does not passivate in 0.5M sulphuric acid as Ti and TiC do [16, 23, 24]. The dissolution of TiB_2 into titanil ions TiO^{2+} and boric acid has been reported in low pH solutions [16]. Furthermore, comparative [11] studies have showed lower corrosion

resistance in acid solutions for TiB_2 compared with other titanium based ceramics such as TiN or Ti(B,N) [22].

Surface modification of titanium and deposition of hard composites based on titanium nitrides or titanium carbides have been widely investigated as a way to overcome the low wear properties of titanium in order to broaden the applications of titanium in biomedical applications [25-28]. In this sense, new application niches for these nanocomposite coatings are of interest due to these excellent properties. TiB_xC_y -based compounds could be of potential use in the food processing industry and in the manufacturing of medical items (scalpels, scissors, tweezers, retractors) where both wear resistance as well as corrosion resistance requirements are quite demanding since they are cyclically submitted to aggressive solutions. Both applications develop in continuous contact with organic material, which acts as preferential sites for the proliferation of bacteria, fungi, yeast and molds responsible for food poisoning and human illness. Cleaning is a very important issue for both applications as these items regularly come in contact with strong oxidizing solutions which are common in disinfectants and sterilizers. Peracetic based solutions are efficient microbicidal agents ensuring the asepsis of the surfaces after cleaning [29, 30], but these solutions are also very corrosive for most of the metals used in food industry and surgical tools and could therefore result in serious economic loss.

Under working conditions that require to be in sliding contact with other materials in a corrosive medium, a synergistic combination of wear and corrosion processes takes place (tribocorrosion), causing more severe degradation than the sum of the individual processes - mechanical and corrosive -separately [31-33]. Although it is very complex to predict the behaviour of materials subjected to tribocorrosion due to several factors involved in the process, the use of electrochemical techniques combined with tribological testing can contribute to an estimate of the contribution of wear and corrosion to the total worn volume [34-36].

Literature reporting the combined effect of the sliding conditions in aggressive media for TiB_xC_y or TiB_2 is scarce. Gorokhovskiy et al. [13] evaluated the corrosion/oxidation resistance of TiCrN/TiCrCN+TiBC (SL and ML) coatings using severe sliding conditions: high load, high temperature in the presence of PFPAAE lubricant. Coated substrates showed minor mechanical wear deformations, no material transference to

testing balls and no visible corrosion sites outside the wear track, while minor corrosion spots were observed at the track, after 200 h of testing. Conversely, the uncoated substrate showed the wear track fully corroded after 200 h, and multiple corrosion sites were visible outside the wear track. In the present work, AISI 316L stainless steel specimens were coated with $\text{TiB}_x\text{C}_y/\text{a-C}$ nanocomposites coatings and their tribocorrosion resistance was evaluated. Tribocorrosion tests were performed in peracetic based solutions in order to explore the potential use of $\text{TiB}_x\text{C}_y/\text{a-C}$ coatings in the food processing industry and for surgical items where the asepsis is a demanding requirement.

2. Experimental

The $\text{TiB}_x\text{C}_y/\text{a-C}$ coatings were prepared by Ar^+ sputtering of a combined $\text{TiC}:\text{TiB}_2$ (60:40) and graphite targets. The magnetrons were connected to radio frequency (graphite target, Goodfellow, 99.5%) and pulsed direct current (d.c.) sources ($\text{TiC}:\text{TiB}_2$ target), at frequencies of 13.56 MHz and 50 kHz, respectively. The pressure of the vacuum chamber was measured in 3×10^{-4} Pa before deposition and set to 0.60 Pa during film growth. The power applied to the $\text{TiC}:\text{TiB}_2$ and graphite targets were 125 and 250 W respectively. Film deposition always began by first sputtering the mixed $\text{TiC}:\text{TiB}_2$ target at 250 W to deposit an adhesion-promoting underlayer during 1 h. Secondly, the magnetron with the graphite target was switched on and set at 250 W for the rest of the deposition. The magnetron heads are tilted by 45° with respect to the vertical axis and placed in a sputtering-down configuration. The substrates were mounted on a rotary sample-holder, placed at 10 cm from the targets. Prior to starting the deposition, an Ar^+ etching of the substrates was performed at 7 Pa and 1000 V (d.c.) for 1 h to remove any adventitious contamination layer. A rotation speed of 10 rpm was used to ensure homogeneity. No intentional heating of the substrate was applied. A negative d.c. bias of 100 V was applied to the samples during the whole deposition process. The total growth time was approximately 5 h and the film thickness was found to be 1 μm . The chemical composition was measured as 61 at.% of C, 14 at.% of B and 25 at.% of Ti. Further details about the synthesis procedure and characteristics of the films can be found in reference [2, 6, 7].

Coupons of AISI 316L (20 x 20 x 3 mm³) and silicon (100) were used as substrates. The steel substrates were ground through successive grades of SiC paper to 1200 grade, and

mirror-polished ($R_a < 0.01 \mu\text{m}$) in diamond paste of $3 \mu\text{m}$. Then, both types of substrates were degreased with a detergent and rinsed in tap water followed by deionised water. Finally, prior to entering into the deposition chamber they were cleaned ultrasonically with acetone and ethanol. The substrate cleaning by wet chemical and ion surface etching processes have been revealed to be critical for a correct performance in tribocorrosion experiment. Inappropriate treatment can lead to a deficient adhesion at the underlayer/substrate interface.

The crystal structure of the films was examined by grazing incidence X-ray diffraction (XRD) using an angle of 5° and Cu $K\alpha$ radiation in a Siemens D5000 diffractometer with parallel beam geometry. A step size of 0.02 (2θ) with 10 s per point were used. Raman measurements were carried out with a LabRAM (Horiba Jobin Yvon) spectrometer equipped with a true confocal microscope, a charge-coupled device detector and a He-Ne laser (532 nm) working at 5 mW to avoid sample damaging. Spectrum was measured with 100 s exposure time and aperture opening of $100 \mu\text{m}$ using a $100\times$ magnification. No background subtraction was applied to the obtained spectrum. The microstructure of the initial coating was evaluated by field emission gun scanning electron microscopy (SEM FEG) Hitachi S4800 equipment at 5 kV. A fracture cross-sectional view was obtained by breaking a deposited silicon wafer.

Electrochemical behaviour of the $\text{TiB}_x\text{C}_y/\text{a-C}$ coatings and reference AISI 316L specimens were analyzed by potentiodynamic polarization curves using a conventional three-electrode cell with a GAMRY Reference 600 potentiostat. An Ag/AgCl (3M KCl) electrode was used as reference electrode, a platinum wire as counter electrode and an exposed area of 0.313 cm^2 and 0.065 cm^2 for the bare AISI 316L and $\text{TiB}_x\text{C}_y/\text{a-C}$ coating respectively as working electrode. After 900 s to allow the stabilization of the open circuit potential, OCP, a cathodic potential step of 300 mV below the OCP is applied. Then, the potential sweep starts anodically at a scan rate of 0.16 mV/s and ends at 1.2 V vs. reference electrode Ag/AgCl or when the current density reaches the limit of 0.25 mA/cm^2 . All tests were carried out in triplicate, at room temperature, in a 1 vol.% of the commercial disinfectant solution named Oxonia (26.0 vol.% in peracetic acid, 18.5 vol.% in hydrogen peroxide, 16.5 vol.% in acetic acid). The pH of the testing solutions was 3.

Tribocorrosion tests of $\text{TiB}_x\text{C}_y/\text{a-C}$ coatings and AISI 316L specimens were carried out using a ball-on-disk configuration with a Microtest MT4000 tribometer in a cell of 100 cm^3 in volume allowing the simultaneous wear and corrosion testing. Prior to any test, specimens were cleaned with a commercial alkaline detergent, rinsed with distilled water and finally wiped with ethanol and dried with warm air. Specimens were then masked with an anticorrosive tape leaving just 0.3 cm^2 of the surface exposed to the test solution. The sliding wear tests were performed under a applied normal load of 2 N, a constant rotation speed of 60 rpm and a track diameter of 3 mm. Corundum balls with a diameter of 3 mm and average roughness (Ra) about 13 nm, were used as counterbody due to their chemical inertness and electrical insulating properties. All tests were performed for 6000 cycles, equivalent to 57 m of sliding distance, and friction coefficient data were recorded during the whole test. After the tests the Ra of the balls keeps in the same range.

Simultaneously to the wear sliding tests, current and potential measurements were carried out in a 1% Oxonia solution. Electrochemical Noise noise measurements is a non-perturbative electrochemical technique that allows for “in situ” gathering of the current and potential variations caused as a result of the sliding of the ball on the disc in the presence of an aggressive environment. An Ag/AgCl (3M KCl) reference electrode was used to record the potential variations by a potentiostat, Gamry Reference 600, by means of the ESA 4000 software. The current fluctuations that naturally occurred during the sliding tests - current noise - are recorded using a platinum counter electrode connected through a zero resistance ammeter –ZRA–. The area of the platinum microelectrode is sufficiently small to avoid the polarization of the working electrode, ensuring that current variations are only the results of the mechanically influenced electrochemical process [37]. In the present case the area of the micro-cathode is 0.05 mm^2 . Potential and current measurements were performed at a sampling rate of 10 Hz to ensure that all the variations related to the tribocorrosion process were gathered. The wear test started ten minutes after the immersion of the samples in the electrolyte in order to let current and potential to stabilize. Then, the counterbody was then immersed in the solution and sliding test started. Fluctuations in potential and current were registered during the 6000 cycles of the wear test and once the sliding test finished, the counterbody was lifted away. Potential and current fluctuations were still recorded for an additional ten minutes.

After the tribocorrosion tests, wear tracks were evaluated by an optical confocal imaging profiler to calculate the worn volume from four sections of each wear scar. Wear rate of the specimens was calculated as the worn material volume normalized by the sliding distance and the normal load applied (mm^3/Nm). The morphology of the surface specimens after corrosion-wear tests were examined by optical microscopy and FEG-SEM microscope (JSM6500F JEOL) at 15 kV of accelerating voltage.

3. Results and Discussion

3.1. Microstructural and chemical characterization

A cross-section view of the $\text{TiB}_x\text{C}_y/\text{a-C}$ coating grown on a silicon substrate is shown in Figure 1. A bilayer structure is observed as a consequence of the previous deposition of an adhesion interlayer formed by single sputtering of mixed $\text{TiC}:\text{TiB}_2$ target of around 300 nm. In the second step the $\text{TiB}_x\text{C}_y/\text{a-C}$ nanocomposite is deposited by switching the graphite target on simultaneously. The microstructure of the $\text{TiB}_x\text{C}_y/\text{a-C}$ coating is observed to be dense with no clear evidence of columnar growth. The crystalline composition was analyzed by means of grazing incidence XRD. The diffractogram shown in Figure 2a reveals a broad band at 35° that is situated between the (100) TiB_2 and (111) TiC planes. Due to its poor crystallinity, by XRD it is difficult to assess the origin of this peak among these different possibilities: a new phase different to TiB_2 or TiC ; a TiC -like phase with some of the C atoms replaced by B; a TiB_2 -like phase with some of the B atoms replaced by C. In fact, the formation of a TiB_xC_y phase by incorporation of carbon into the TiB_2 phase was demonstrated previously by x-ray absorption near edge spectroscopy for C contents < 50 at.% . The structure evolved from distorted-hexagonal to cubic-like as the carbon content further increased [6, 7, 38]. The average crystallite size was estimated to be 2-3 nm from the broadening of the main peak using the Scherrer formula. The existence of an amorphous carbon bonded-matrix is confirmed by Raman spectroscopy. The two peaks characteristic of the sp^2 sites of all disordered carbons at 1350 (D-peak) and ordered graphite at 1585 cm^{-1} (G peak) are observed in Figure 2b. The features at lower wavenumbers are due to the Raman scattering of Ti-C bonds in disordered TiC_x compounds [38]. The fraction of C atoms present in this a-C phase has been estimated to be 41 at.% by x-ray photoelectron spectroscopy [6] and the electrical resistivity to be $428 \mu\Omega\cdot\text{cm}$ [38]. Summarizing the

obtained chemical composition and bonding data, the deposited material can be defined as a nanocomposite material formed by nanocrystals of $\text{TiB}_{0.6}\text{C}_{1.4}$ surrounded by a-C phase ($X_{\text{a-C}} = 41 \text{ at.}\%$).

3.2. Corrosion behaviour

Figure 3 compares the potentiodynamic polarization curves corresponding to uncoated and coated AISI 316L specimens in 1% Oxonia solution. The curve corresponding to pure titanium has also been included for comparison purposes. The corrosion potential of the $\text{TiB}_x\text{C}_y/\text{a-C}$ specimen is about 0.234 V vs. Ag/AgCl, while the uncoated stainless steel shows a nobler corrosion potential, 0.375 V vs. Ag/AgCl. The anodic branch of both curves is not fully vertical but displays a high slope meaning a low rate for the metal dissolution reaction. Similarly, the cathodic branch also describes a negative slope. Thus, the shape of the potentiodynamic curves indicates an activation control of the corrosion process and a continuous but slow dissolution of the TiB_xC_y layer and AISI 316L therefore takes place in this media. The length of the anodic branch is larger for the $\text{TiB}_x\text{C}_y/\text{a-C}$ than for AISI 316L. For the coated specimens the change of the slope occurred at 1.040 V vs. Ag/AgCl corresponding to the water decomposition and O_2 evolution, while for the bare stainless steel, the change observed at 0.690 V vs. Ag/AgCl corresponds to limit of predominance of the dissolved species varying from Cr^{3+} to $\text{Cr}_2\text{O}_7^{2-}$.

Despite these differences, corrosion current density, i_{corr} , is quite similar in both cases. The i_{corr} values, estimated by the intersection of the Tafel slopes, Figures. 3b and 3c, show values ranging about 10^{-7} A/cm^2 , either for $\text{TiB}_x\text{C}_y/\text{a-C}$ coated steel or for the bare AISI 316L.

Literature reporting the electrochemical behaviour of TiB_xC_y coatings is scarce so the interpretation of the results, therefore, is based on the behaviour of Ti compounds. According to the Pourbaix diagram for pure titanium [23] at the pH=3 of the testing solution, 1% Oxonia, the stable compound is $\text{TiO}_2 \cdot \text{H}_2\text{O}$. The range of stability of this compound is quite large, so at the whole potential sweep plotted in the polarization curve pure titanium would be passive, as it can be seen by the reverse anodic scan shown in Figure 3. **Hintermann et al. [24] studied the corrosion and passivation of TiC prepared by CVD in sulphuric acid solutions. These authors established the anodic processes, identifying that the corrosion process occurs with the formation of TiO^{2+} ,**

with Ti^{3+} as an intermediate, followed by either the evolution of carbon dioxide or carbon monoxide; while passivation is the result of the progressive covering of the surface by $TiO_2 \cdot H_2O$. Finally, the authors described a Pourbaix diagram for the modified system $TiC \cdot H_2O$, showing a passive state at this acidic solution.

On the other hand, titanium diboride TiB_2 has been extensively studied in acid and neutral media [16-22]. Covino et al. [16], studied the electrochemical behaviour of TiB_2 in oxygen-aerated sulphuric acid solution. In this strong acid medium, they observed that TiB_2 dissolved stoichiometrically as Ti^{3+} and boric acid indicating that 10 to 40% of the dissolved titanium occurred as titanous ions, the remainder occurred as titanyl ions. In a second stage titanous ions react with water to form titanyl ions. Passivation by the formation of the hydrated TiO_2 oxide is strongly dependent on the critical concentration of titanyl ions reached on the surface at the low pH. The presence of the Ti^{3+} ions as an intermediate product of the reaction appears to modify the equilibrium line leading to a high solubility of the oxide layer in strongly acidic solution.

Andreev et al. [39], performed a depth study on the electrochemical corrosion behaviour of dense composite materials, based on TiC . In this work they observed that the $Ti:C$ stoichiometry significantly affects corrosion rate. The $TiC_{0.47}$ stoichiometry exhibited four or five times corrosion rate than the $TiC_{0.98}$. Moreover, they also determined that increasing the volume fraction of TiB_2 in $TiC-TiB_2$ composites the corrosion resistance decreased, and those composites containing in excess of 40% TiC exhibited the highest corrosion resistance. The 80% TiC -20% TiB_2 composite is particularly attractive because of the favourable combination of hardness and corrosion resistance.

According to them the TiO_2 formed on the surface of the $TiC_{0.98}$ film is the responsible for the corrosion resistance. The presence of this passivating film will impede carbide dissolution and, therefore, the corrosion rate of the film will be determined by the diffusion through the oxide film. On the other hand, the preferential dissolution of the TiB_2 and/or the TiB_2-TiC interface is mentioned as the cause of the black pores formed.

Additionally, they also studied the influence of the cristallinity concluding that the corrosion resistance of these composites deposited as thin film showed lower corrosion rate than in bulk material. The micro-crystalline structure in the sputtered film is

thought to be the main reason for the significant decrease in corrosion rate compared with the corresponding SHS-synthesized target material.

Even though the comparison of the corrosion rate of the TiB_xCy/a-c coating with respect to the values reported in the literature [24, 39], cannot be so straightforward since the corrosion tests were not performed in the same conditions, it can be stated that the corrosion resistance for the TiB_xCy/a-C is at least two order of magnitude higher.

On the other hand, it is well known that a-c: H films have several applications in different industrial areas, because of their high density, hardness and chemical inertness. Although the film characteristics depend on deposition parameters, it is well accepted that the higher sp³ C structures, the higher the chemical resistance. Mansano et al.[40] studied the exposure of these films to different acid and alkaline solutions. By means of Raman spectroscopy they observed that only the exposure of a-c:H films to hydrofluoric acid –a reductive acid- promoted a degradation of the sp³ C-H bonds, and as consequence, a reduction in the quality of the films i.e. an increase in the current level recorded during the voltammetric tests resulted of corrosion processes.

Therefore, the presence of a new intermediate phase between the TiC and the TiB₂ of nanometric size appears to be the reason for a better corrosion behaviour than the TiB₂ and slightly lower than pure titanium and titanium carbide at this pH range.

Even though there is no reference in the literature about the potential–pH equilibrium diagram for the TiB_xCy /a-C system it appears that the growth of a hydrated TiO₂ layer may also occurs during the anodic polarization in 1% Oxonia acid medium although the stability of the grown oxide is slightly lower than that described for pure titanium. The reaction of the boron with water to form boric acid and Ti³⁺ may slightly modify the equilibrium line increasing the activity of the TiB_xCy regarding pure Ti and TiC. This increase in the electrochemical activity by the incorporation of B to form a ternary compound has been previously reported in the literature for different TiBN [22, 39]. Holleck suggested that the nature of the chemical bonding character influences the stability of the compound and corrosion resistance [41, 42]. The metallic nature of the chemical bonding of titanium hard coatings (nitrides, carbides, borides) increases from nitrides to borides. Therefore, the stability of TiB₂ is lower than TiC, and thus the stability of TiB_xCy ranges in-between [41].

3.3 Tribocorrosion behaviour

The sliding tests performed in the oxidizing solution revealed that the coefficient of friction (COF) for the $\text{TiB}_x\text{C}_y/\text{a-C}$ coatings is notably reduced compared to that for stainless steel. Figure 4 displays the friction curves for three different $\text{TiB}_x\text{C}_y/\text{a-C}$ coated samples prepared in different batches and the bare substrate tested under identical conditions. A defective coating showing lack of adhesion, labelled with (*), is included for a comparative analysis.

While AISI 316L shows COF values about 0.6, the coated specimens show COFs about 0.1-0.2. The higher COF value recorded for the $\text{TiB}_x\text{C}_y/\text{a-C}$ (*) appears to point out some differences in comparison with the other two specimens. Values from 0.1-0.2 were also obtained on dry sliding of $\text{TiB}_x\text{C}_y/\text{a-C}$ against WC-Co and 100Cr6 steel balls at loads of 1 and 5 N [5-7], indicating that these low values can also be achieved in wet conditions.

The electrochemical noise measurements (potential and current fluctuations) recorded simultaneously during the sliding test for the $\text{TiB}_x\text{C}_y/\text{a-C}$ coated specimens are shown in Figure 5. For comparison purposes the current and voltage fluctuations for the bare substrate have also been included. Three different stages are clearly distinguished, (cf. Figure 5a). Initially, current and voltage are recorded for 10 minutes under static conditions without applying any load, both records show steady values over time (stage I). Afterwards, an abrupt decrease in potential towards more cathodic values, as well as an increase in the current occur at the onset of the sliding under loading conditions, (stage II). This decrease in potential and simultaneous increase in current are related with the activation of the surface as a result of the removal or thinning of the native oxide layer caused by the mechanical damage. Finally, at the end of the sliding and load removal, stage III, the values of potential and current reach similar values as at the beginning, i.e. before the sliding stage.

Nonetheless, despite the fact that deposition conditions were the same for all the $\text{TiB}_x\text{C}_y/\text{a-C}$ coated specimens; it was possible to observe some significant differences in the potential and current fluctuations among samples. Figure 5c and 5d, illustrates an example of a defective $\text{TiB}_x\text{C}_y/\text{a-C}$ (*) specimen. A more pronounced potential shift

towards cathodic values and higher values for the current during the sliding stage regarding pristine $\text{TiB}_x\text{C}_y/\text{a-C}$ coatings, and even for the bare steel, were observed. This potential shift, towards more negative values is caused by the exposure of bare steel to the electrolyte through the defects leading to the onset of a galvanic coupling. This increases the corrosion rate with respect to the pristine coating. At the same time, the wear track becomes larger, so the bare steel area too. As result of that, the anode/cathode area ratio within the track decreases, and the galvanic coupling becomes severer. So the coating within the track dissolves faster, and the current recorded is higher.

The galvanic coupling hinders the repassivation of the coating in the track. Such active dissolution shifts the potential towards more active region, thus, the surface turns prone to oxidize.

After the completion of the tribocorrosión test, wear tracks were carefully examined by optical microscopy and SEM. The wear tracks on $\text{TiB}_x\text{C}_y/\text{a-C}$ coatings were hardly visible (cf. Figure 6a), characteristic of a mild wear. Conversely, the defective specimen $\text{TiB}_x\text{C}_y/\text{a-C}$ (*) shows cracks and delaminated areas at the edge of the wear track as can be seen in Figures 6c and 6d. Such cracks appear to be oriented along the sliding direction and the delaminated areas are at the edge of the wear tracks. These features are distinctive of the brittle layers described by Gorokovsky et al. [14] on multilayered $\text{TiCrN}+\text{TiBC}$ coatings where the most external layer cracked and delaminated after repetitive sliding wear. Sánchez-López et al. also observed that the wear resistance of the $\text{TiB}_x\text{C}_y/\text{a-C}$ was lower than $\text{TiC}/\text{a-C}$ and $\text{WC}/\text{a-C}$ composites despite their higher hardness and attributed to their higher brittleness [43]. This local delamination also explains the higher COF values (Figure 4) and the increase in the electrochemical activity recorded during the tribocorrosion tests in comparison with the defect-free $\text{TiB}_x\text{C}_y/\text{a-C}$ coating. As a result of the cracking, the underneath substrate is also exposed to the aggressive solution in some sites forming a galvanic couple between the coating and the substrate, enhancing the electrochemical activity of the coating with respect to the pristine. The higher current density recorded in Figure 5d, one order of magnitude higher than for pristine specimens, indicates that both the active area, increases and, the coating in the track is being anodically polarized by the surrounding bare steel. Therefore the current recorded in this case is higher than for the steel specimen and the pristine specimen, respectively.

The profiles and topographical views of the wear track on AISI 316L and $\text{TiB}_x\text{C}_y/\text{a-C}$ specimens are shown in Figure 7. It can be clearly seen that the wear track is wider and deeper on AISI 316L than on $\text{TiB}_x\text{C}_y/\text{a-C}$ coated specimens. The wear rate for the coated specimens are one order of magnitude lower than AISI 316L, about $4 \cdot 10^{-6} \text{ mm}^3/\text{Nm}$ vs. $4 \cdot 10^{-5} \text{ mm}^3/\text{Nm}$, respectively. These wear rates are in agreement with those reported in previous works in dry sliding wear tests [5-7], suggesting that the exposure to the oxidizing solution does not seem to influence greatly the wear rate. The good behaviour shown by the coated specimens in comparison to the stainless steel suggests that $\text{TiB}_x\text{C}_y/\text{a-C}$ coatings should be suitable for food processing and biomedical applications. In summary, the adequate balance between tribological and corrosion properties makes this nanocomposite $\text{TiB}_x\text{C}_y/\text{a-C}$ material very interesting since in previous works duplex systems combining an insulating and a DLC layer were used to achieve the multifunctionality [11].

4. Conclusions

Electrochemical tests performed on $\text{TiB}_x\text{C}_y/\text{a-C}$ nanocomposite coating has determined a corrosion current density ranging on the same order as that for bare AISI 316L; however it presents a notable decrease in the COF (0.1 vs. 0.6), a reduction in the wear rate of one order of magnitude, and a longer pseudo passive stage. The presence of a new phase as well as their compact microstructure prevents galvanic coupling with the substrate, since the coating behaves as a barrier layer. Therefore, a $\text{TiB}_x\text{C}_y/\text{a-C}$ nanocomposite coating notably improves the tribological properties of the AISI 316L without a deleterious effect on corrosion resistance in strong oxidant solutions composed of acetic, peracetic and hydrogen peroxide. $\text{TiB}_x\text{C}_y/\text{a-C}$ nanocomposite material appears to be as an interesting protective tribological coating for the biomedical and food sectors. This represents an advantage over previous works where duplex systems were used to achieve the multifunctionality.

Acknowledgements

The Spanish MEC (projects n° MAT2007-66881-C02-01; MAT2011-29074-C02-01 and CONSOLIDER FUNCOAT CSD2008-00023) and Junta de Andalucía (P10-TEP-6782) are acknowledged for financial support.

References

- [1] S. Vepřek, The search for novel, superhard materials, *J. Vac. Sci. Technol.* 17 (1999) 2401-2420.
- [2] S. Zhang, D. Sun, Y. Fu, H. Du, Recent advances of superhard nanocomposite coatings: a review, *Surf. Coat. Technol.* 167 (2003) 113-119.
- [3] A.A. Voevodin, J.P. O'Neill, J.S. Zabinski, Nanocomposite tribological coatings for aerospace applications, *Surf. Coat. Technol.* 116–119 (1999) 36-45.
- [4] T.S.R.C. Murthy, B. Basu, A. Srivastava, R. Balasubramaniam, A.K. Suri, Tribological properties of TiB₂ and TiB₂-MoSi₂ ceramic composites, *J. Eur. Ceram. Soc.* 26 (2006) 1293-1300.
- [5] J.C. Sánchez-López, M.D. Abad, A. Justo, R. Gago, J.L. Endrino, A. García-Luis, M. Brizuela, Phase composition and tribomechanical properties of Ti-B-C nanocomposite coatings prepared by magnetron sputtering, *J. Phys. D: Appl. Phys.* 45 (2012).
- [6] M.D. Abad, D. Cáceres, Y.S. Pogozhev, D.V. Shtansky, J.C. Sánchez-López, Bonding structure and mechanical properties of Ti-B-C coatings, *Plasma Process. Polym.* 6 (2009) S107-S112.
- [7] M.D. Abad, J.C. Sánchez-López, M. Brizuela, A. García-Luis, D.V. Shtansky, Influence of carbon chemical bonding on the tribological behavior of sputtered nanocomposite TiBC/a-C coatings, *Thin Solid Films* 518 (2010) 5546-5552.
- [8] P. Papakonstantinou, J.F. Zhao, P. Lemoine, E.T. McAdams, J.A. McLaughlin, The effects of Si incorporation on the electrochemical and nanomechanical properties of DLC thin films, *Diamond. Relat. Mater.* 11 (2002) 1074-1080.
- [9] H.-G. Kim, S.-H. Ahn, J.-G. Kim, S. Jun Park, K.-R. Lee, Corrosion performance of diamond-like carbon (DLC)-coated Ti alloy in the simulated body fluid environment, *Diamond. Relat. Mater.* 14 (2005) 35-41.
- [10] M.L. Morrison, R.A. Buchanan, P.K. Liaw, C.J. Berry, R.L. Brigmon, L. Riestler, H. Abernathy, C. Jin, R.J. Narayan, Electrochemical and antimicrobial properties of diamondlike carbon-metal composite films, *Diamond. Relat. Mater.* 15 (2006) 138-146.
- [11] D. Pech, N. Schupp, P. Steyer, T. Hack, Y. Gachon, C. Héau, A.-S. Loir, J.C. Sánchez-López, Duplex SiCN/DLC coating as a solution to improve fretting—Corrosion resistance of steel, *Wear* 266 (2009) 832-838.

- [12] L. Wang, J.F. Su, X. Nie, Corrosion and tribological properties and impact fatigue behaviors of TiN- and DLC-coated stainless steels in a simulated body fluid environment, *Surf. Coat. Technol.* 205 (2010) 1599-1605.
- [13] V. Gorokhovskiy, C. Bowman, P. Gannon, D. VanVorous, A.A. Voevodin, A. Rutkowski, Tribological performance of hybrid filtered arc-magnetron coatings. Part II: Tribological properties characterization, *Surf. Coat. Technol.* 201 (2007) 6228-6238.
- [14] V.I. Gorokovskiy, C. Bowman, P.E. Gannon, D. VanVorous, A.A. Voevodin, C. Muratore, Y.S. Kang, J.J. Hu, Deposition and characterization of hybrid filtered arc/magnetron multilayer nanocomposite cermet coatings for advanced tribological applications, *Wear* 265 (2008) 741-755.
- [15] V. Gorokhovskiy, C. Bowman, P. Gannon, D. VanVorous, A.A. Voevodin, A. Rutkowski, C. Muratore, R.J. Smith, A. Kayani, D. Gelles, V. Shutthanandan, B.G. Trusov, Tribological performance of hybrid filtered arc-magnetron coatings: Part I: Coating deposition process and basic coating properties characterization, *Surf. Coat. Technol.* 201 (2006) 3732-3747.
- [16] B.S. Covino Jr, S.D. Cramer, J.P. Carter, D. Schlain, Corrosion of titanium diboride, *J. Less. Com. Met.* 41 (1975) 211-224.
- [17] R. Ali, E. Alkhateeb, F. Kellner, S. Virtanen, N. Popovska-Leipertz, Chemical vapor deposition of titanium based ceramic coatings on low carbon steel: Characterization and electrochemical evaluation, *Surf. Coat. Technol.* 205 (2011) 5454-5463.
- [18] E. Alkhateeb, R. Ali, S. Virtanen, N. Popovska, Electrochemical evaluation of the corrosion behavior of steel coated with titanium-based ceramic layers, *Surf. Coat. Technol.* 205 (2011) 3006-3011.
- [19] C. Monticelli, A. Frignani, A. Bellosi, G. Brunoro, G. Trabanelli, The corrosion behaviour of titanium diboride in neutral chloride solution, *Corr. Sci.* 43 (2001) 979-992.
- [20] V.A. Shvets, V.A. Lavrenko, V.I. Subbotin, V.N. Talash, L.I. Kuznetsova, Anodic oxidation of SiC-TiB 2-B 4C composites in 3% NaCl solution, *Powder Metallurgy and Metal Ceramics* 49 (2011) 702-706.
- [21] A.D. Verkhoturov, M.A. Kuzenkova, N.V. Lebukhova, I.A. Podchernyaeva, Electrochemical behavior of transition metals and refractory compounds of titanium in synthetic sea water, *Soviet Powder Metall. Metal. Ceram.* 27 (1988) 162-166.
- [22] B. Matthes, E. Broszeit, J. Aromaa, H. Ronkainen, S.P. Hannula, A. Leyland, A. Matthews, Corrosion performance of some titanium-based hard coatings, *Surf. Coat. Technol.* 49 (1991) 489-495.
- [23] M. Pourbaix, *Atlas d'équilibres Électrochimiques*, PARIS, 1963.
- [24] H.E. Hintermann, A.C. Riddiford, R.D. Cowling, J. Malyszko, The anodic behaviour of titanium carbide in sulphuric acid solutions, *Electrodeposition surf. Treat.* 1 (1972) 59-69.

- [25] M. Azzi, J.A. Szpunar, Tribo-electrochemical technique for studying tribocorrosion behavior of biomaterials, *Biomol. Eng.* 24 (2007) 443-446.
- [26] C. Monticelli, F. Zucchi, A. Tampieri, Triboelectrochemical behaviour of a Si₃N₄-TiN ceramic composite and a titanium alloy commonly used in biomedical applications, *Wear* 266 (2009) 327-336.
- [27] Ç. Albayrak, İ. Hacısalihoğlu, S. Yenal vangölü, A. Alsaran, Tribocorrosion behavior of duplex treated pure titanium in Simulated Body Fluid, *Wear* 302 (2013) 1642-1648.
- [28] S. Mischler, S. Ayrault, D. Landolt, Investigation of tribocorrosion of TiC coatings using electrochemical techniques, *Mater. Sci. Forum* 247 (1997) 9-18.
- [29] Q. Qu, S. Jiang, L. Li, W. Bai, J. Zhou, Corrosion behavior of cold rolled steel in peracetic acid solutions, *Corr. Sci.* 50 (2008) 35-40.
- [30] B. Guitián, X.R. Nóvoa, B. Puga, Electrochemical Impedance Spectroscopy as a tool for materials selection: Water for haemodialysis, *Electrochim. Acta* 56 (2011) 7772-7779.
- [31] X.Y. Wang, D.Y. Li, Investigation of the Synergism of Wear and Corrosion Using an Electrochemical Scratch Technique, *Tribology Letters* 11 (2001) 117-120.
- [32] S.W. Watson, F.J. Friedersdorf, B.W. Madsen, S.D. Cramer, Methods of measuring wear-corrosion synergism, *Wear* 181-183, Part 2 (1995) 476-484.
- [33] R.J.K. Wood, Tribocorrosion, in: *Shreir's Corrosion*, 2010, pp. 1005-1050.
- [34] P.-Q. Wu, J.P. Celis, Electrochemical noise measurements on stainless steel during corrosion-wear in sliding contacts, *Wear* 256 (2004) 480-490.
- [35] R.J.K. Wood, J.A. Wharton, A.J. Speyer, K.S. Tan, Investigation of erosion-corrosion processes using electrochemical noise measurements, *Tribology International* 35 (2002) 631-641.
- [36] P. Ponthiaux, F. Wenger, D. Drees, J.P. Celis, Electrochemical techniques for studying tribocorrosion processes, *Wear* 256 (2004) 459-468.
- [37] A. Aballe, A. Bautista, U. Bertocci, F. Huet, Measurement of the noise resistance for corrosion applications, *Corr. Sci.* 57 (2001) 35-42.
- [38] M.D. Abad, R. Sanjinés, J.L. Endrino, R. Gago, J. Andersson, J.C. Sánchez-López, Identification of Ternary Phases in TiBC/a-C Nanocomposite Thin Films: Influence on the Electrical and Optical Properties, *Plasma Process. Polym.* 8 (2011) 579-588.
- [39] Y. Andreev, E.A. Levashov, A. Sheveiko, V.I. Kosianin, J.J. Moore, D.L. Olson, Electrochemical corrosion behavior of SHS-synthesized d.c. magnetron composite TiC-based targets and sputtered thin films, *Surf. Coat. Technol.* 90 (1997) 42-52.
- [40] R.D. Mansano, M. Massi, A.P. Mousinho, L.S. Zambom, L.G. Neto, Protective carbon layer for chemical corrosion of stainless steel, *Diamond. Relat. Mater.* 12 (2003) 749-752.
- [41] H. Holleck, Material selection for hard coatings, *J. Vac. Sci. Technol.* 4 (1986) 2661-2669.

[42] H. Holleck, Basic principles of specific applications of ceramics Materials as protective layers, Surf. Coat. Technol. 43744 (1990) 245-258.

[43] J.C. Sánchez-López, D. Martínez-Martínez, M.D. Abad, A. Fernández, Metal carbide/amorphous C-based nanocomposite coatings for tribological applications, Surf. Coat. Technol. 204 (2009) 947-954.

Figure captions

Figure 1. SEM cross section of the $\text{TiB}_x\text{C}_y/\text{a-C}$ coating.

Figure 2. a) Grazing angle XRD diffraction pattern. TiC (32-1383), TiB_2 (075-0967) and Fe (01-1262) peak positions are marked above for comparison purposes; b) Raman spectrum of the $\text{TiB}_x\text{C}_y/\text{a-C}$ coating.

Figure 3. a) Potentiodynamic polarization curves of bare AISI 316L, $\text{TiB}_x\text{C}_y/\text{a-C}$ coated stainless steel and pure titanium in 1% Oxonia solution. Tafel slopes plotted on: b) $\text{TiB}_x\text{C}_y/\text{a-C}$ specimen; c) AISI 316L.

Figure 4. Coefficient of friction recorded during the sliding tribocorrosion tests of uncoated and three coated specimens with $\text{TiB}_x\text{C}_y/\text{a-C}$, AISI 316L against corundum ball in 1% Oxonia solution.

Figure 5. Electrochemical noise measurements recorded during the tribocorrosion test against a corundum ball in 1% Oxonia solution: potential (a) and current (b) fluctuations, corresponding to $\text{TiB}_x\text{C}_y/\text{a-C}$ specimens and AISI 316L; potential (c) and current (d) fluctuations corresponding to a defective $\text{TiB}_x\text{C}_y/\text{a-C}$ (*) coating.

Figure 6. a) SEM images of the wear track corresponding to pristine $\text{TiB}_x\text{C}_y/\text{a-C}$ specimens; b) optical image of the wear track corresponding to bare AISI 316L. Wear track corresponding to a defective coating, - $\text{TiB}_x\text{C}_y/\text{a-C}$ (*): c) General view; d) wear track at higher magnifications; e) detail of a delaminated area of the track.

Figure 7. a) Representative wear track profiles for pristine $\text{TiB}_x\text{C}_y/\text{a-C}$ coated specimens and AISI 316L specimens. Topographical views of a section of the wear track corresponding to: AISI 316L (b); a wear-resistant (c) and defective $\text{TiB}_x\text{C}_y/\text{a-C}$ (*) coatings (d).

Figure

[Click here to download Figure: A.Conde_TIBC_Figure- 01-R1.doc](#)

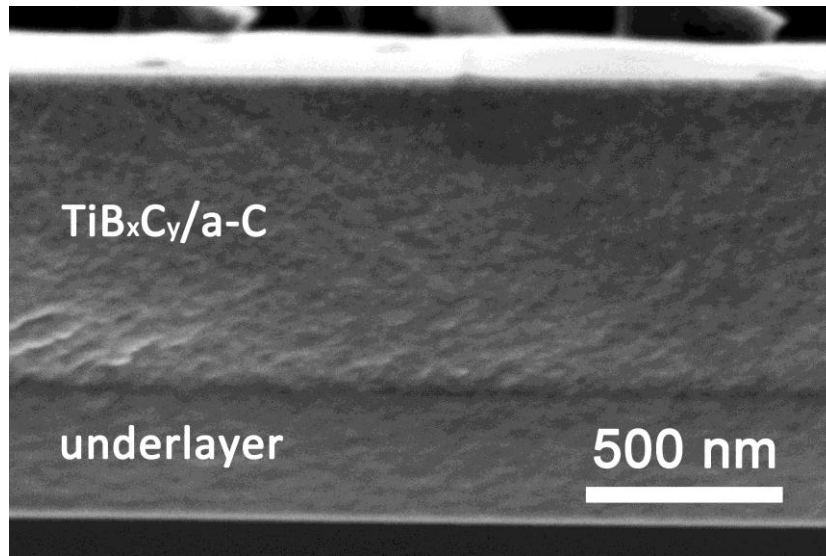


Figure 1.

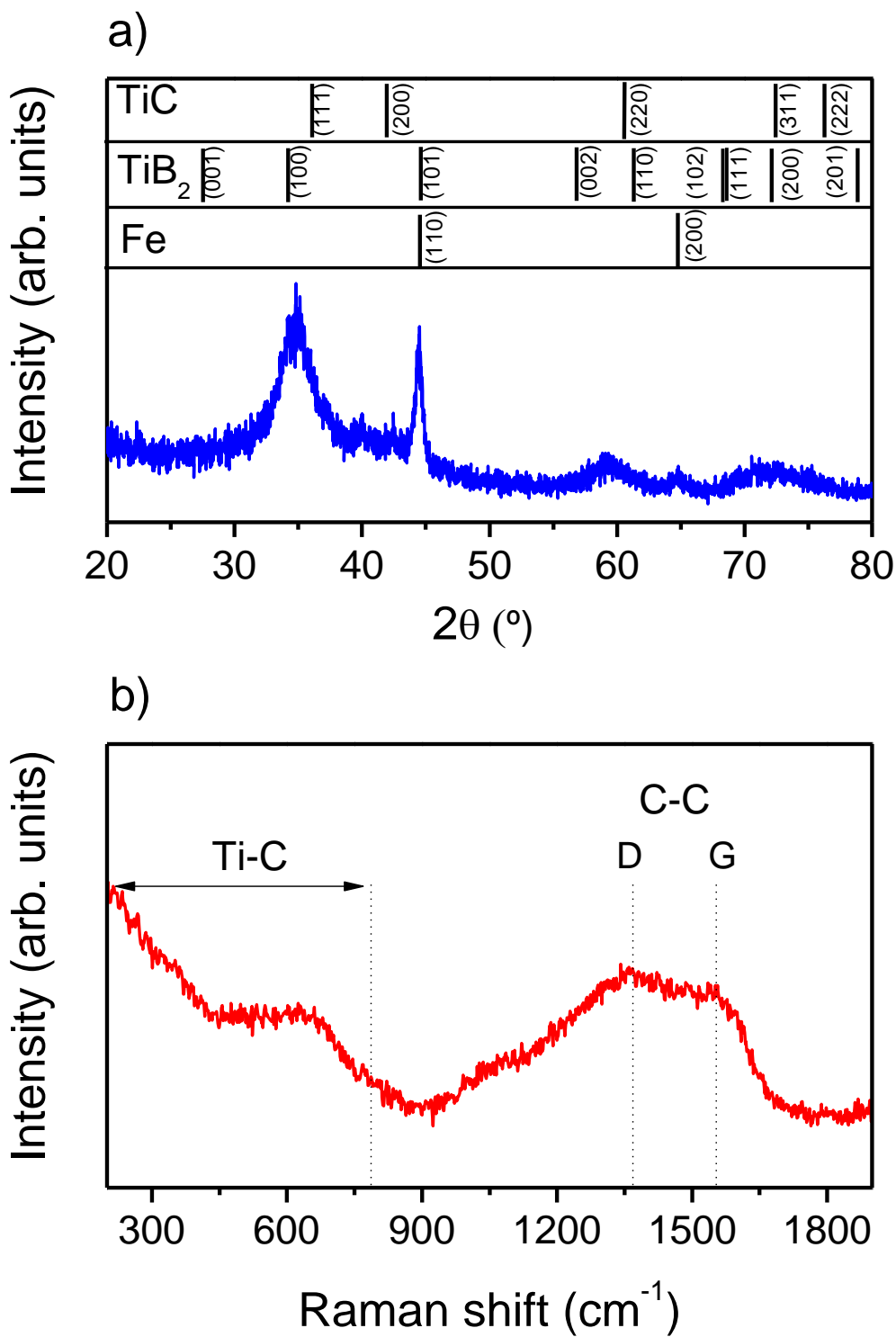


Figure 2

Figure

[Click here to download Figure: A.Conde_TIBC_Figure-03-R2.doc](#)

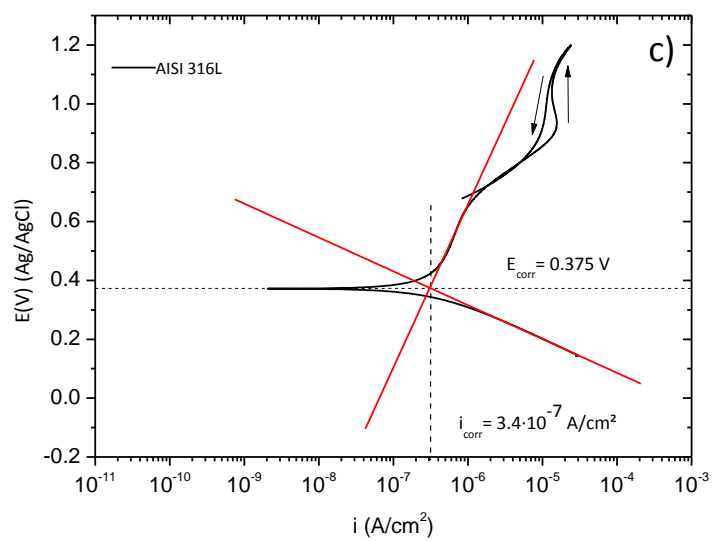
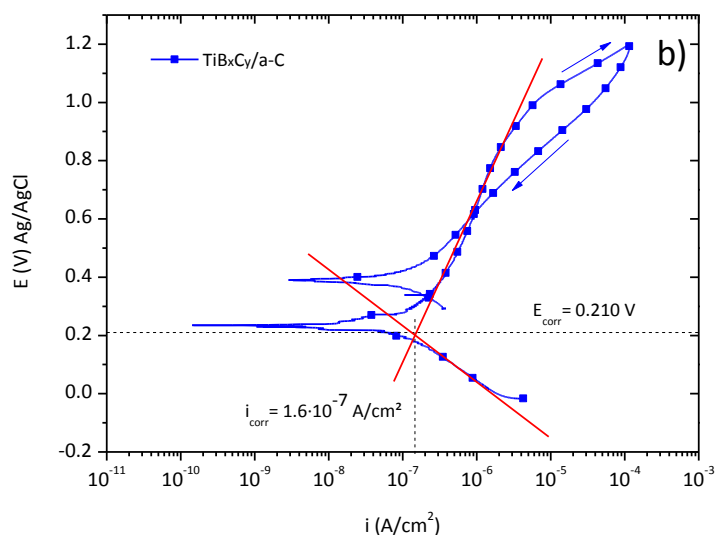
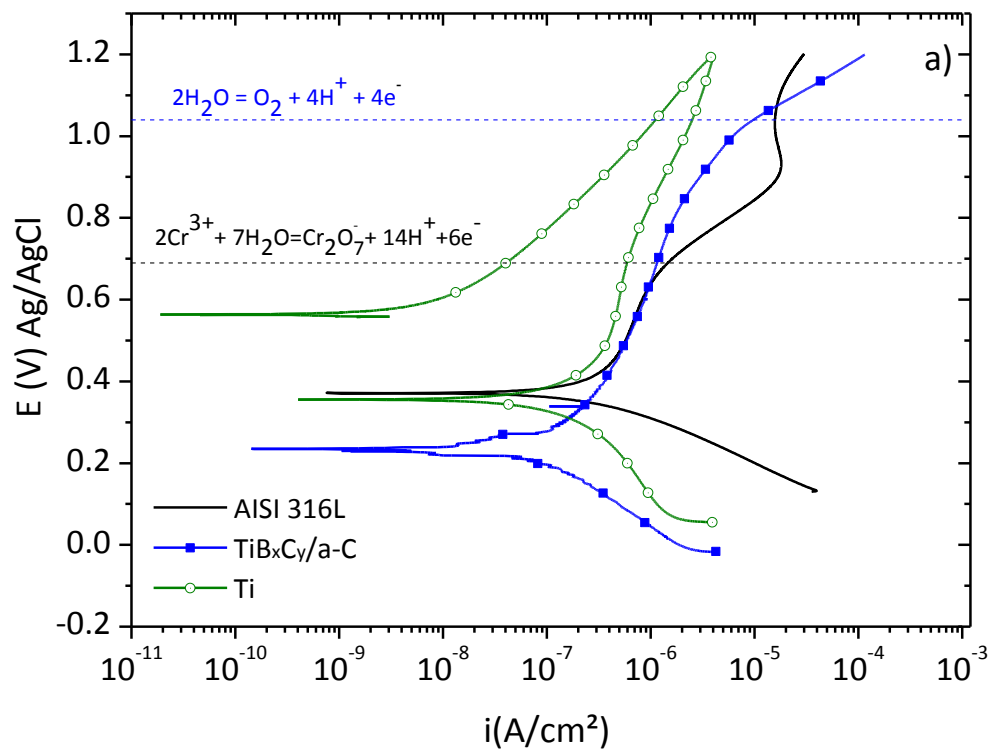


Figure 3

Figure

[Click here to download Figure: A.Conde_TIBC_Figure-04-R2.doc](#)

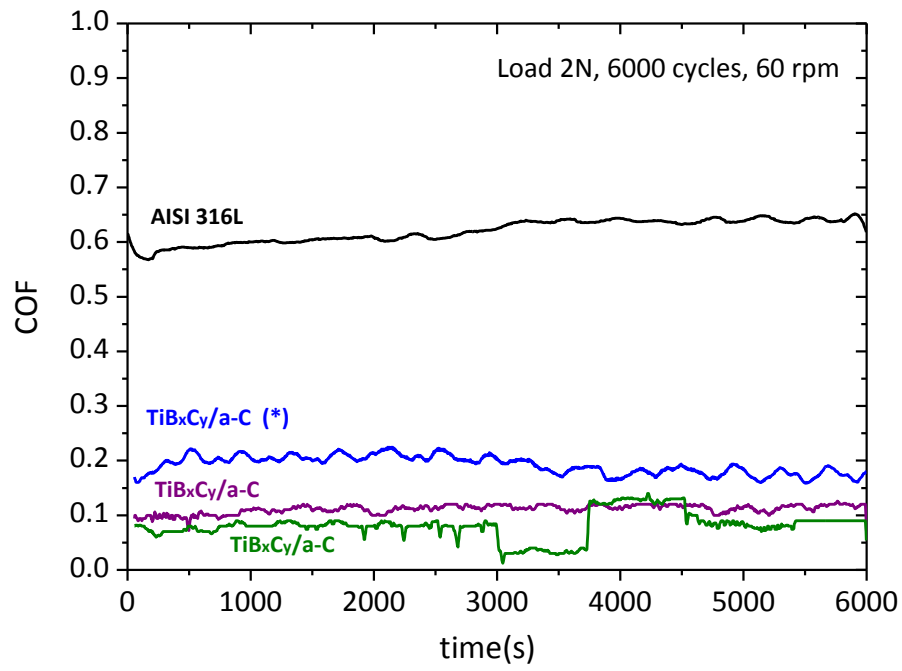


Figure 4

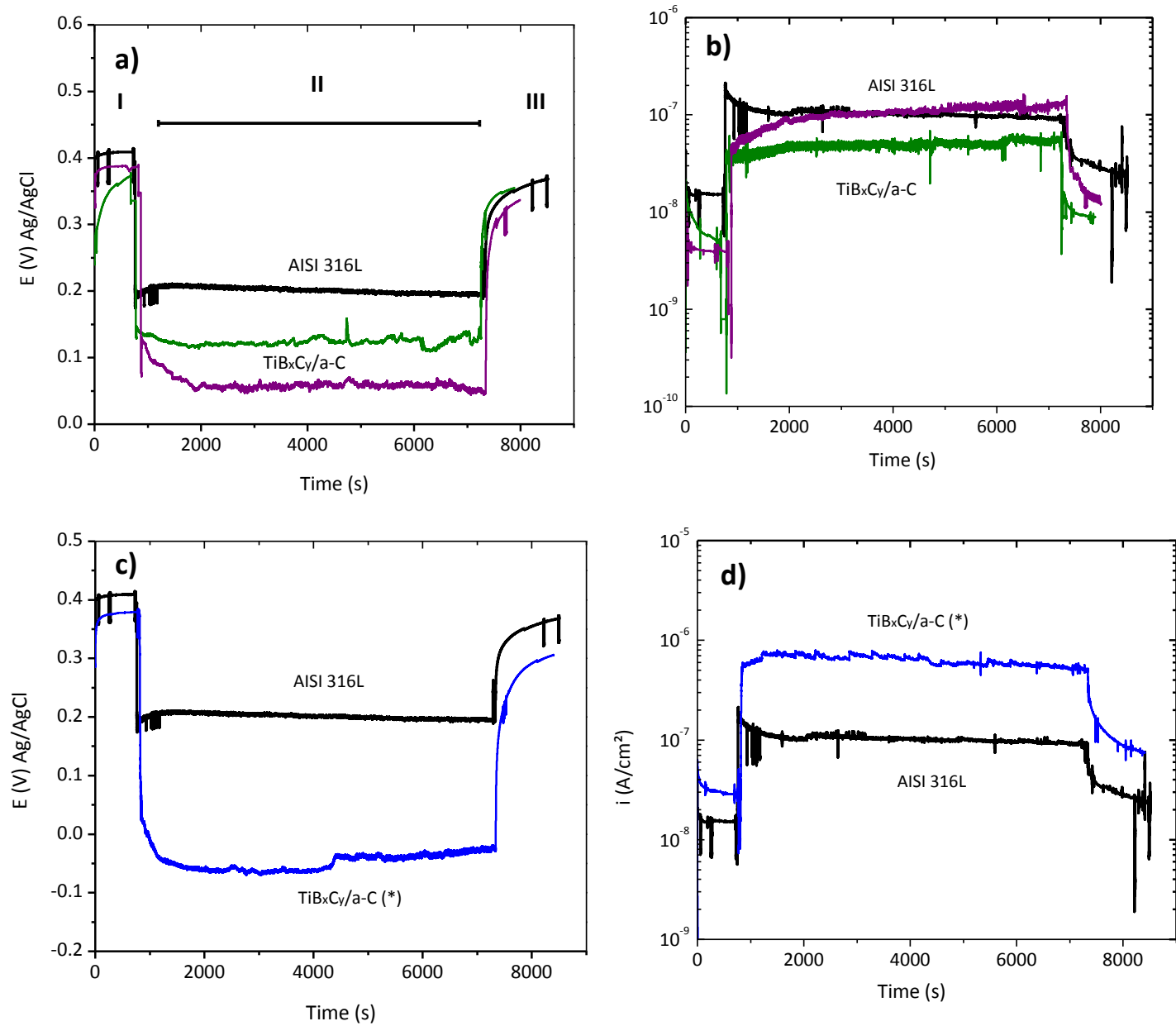


Figure 5

Figure

[Click here to download Figure: A.Conde_TIBC_Figure-06-R1.doc](#)

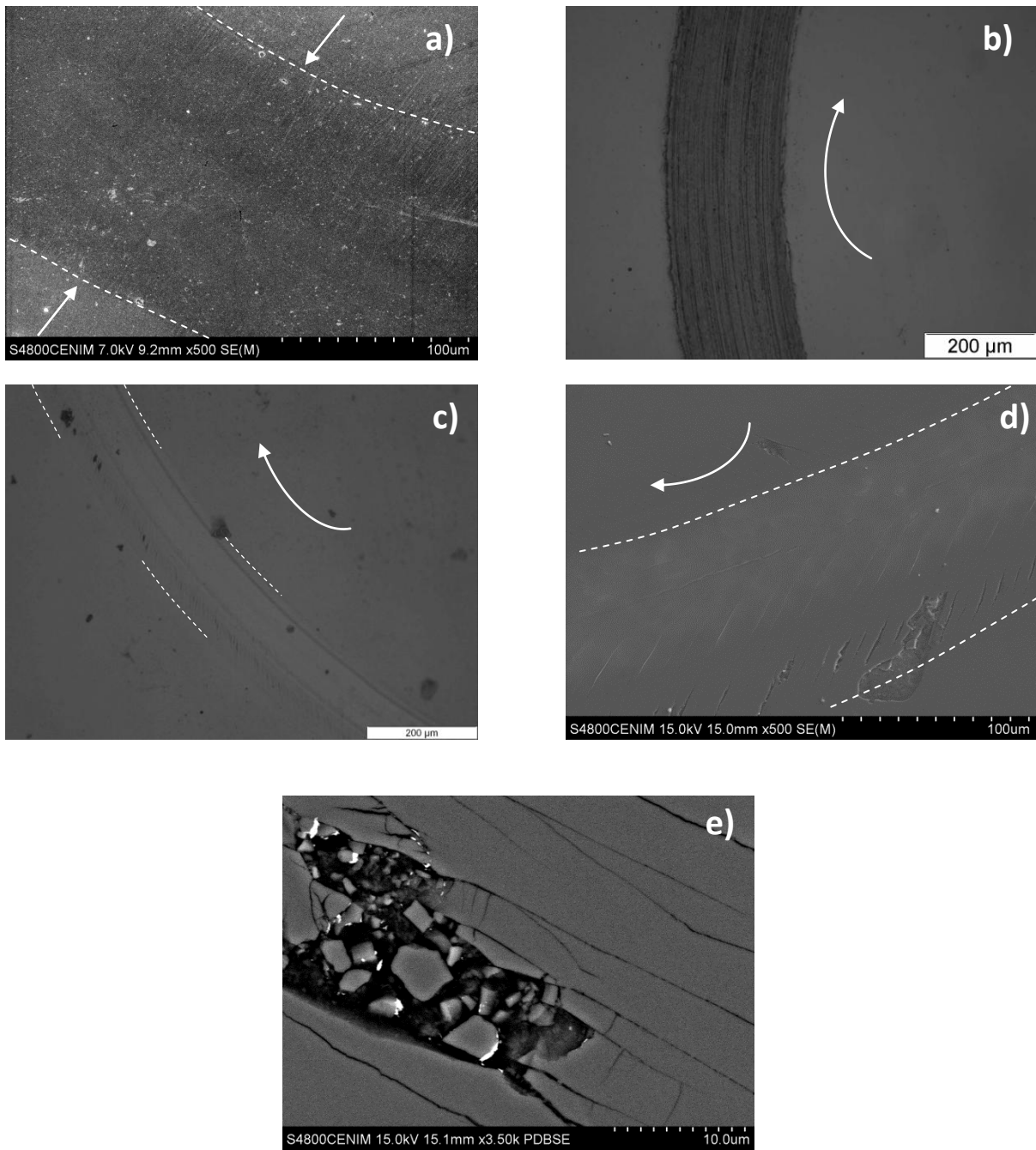


Figure 6

Figure

[Click here to download Figure: A.Conde_TIBC_Figure-07-R1.doc](#)

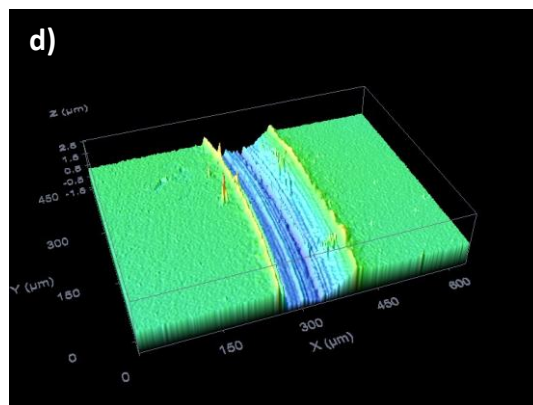
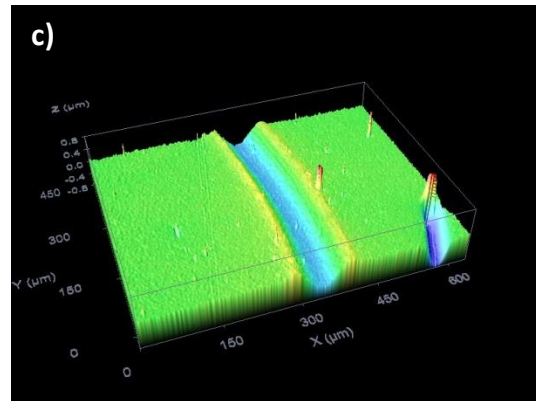
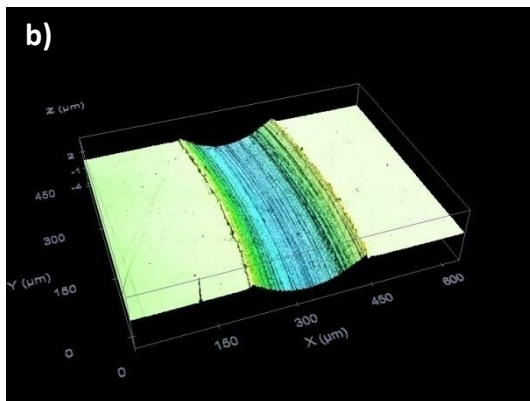
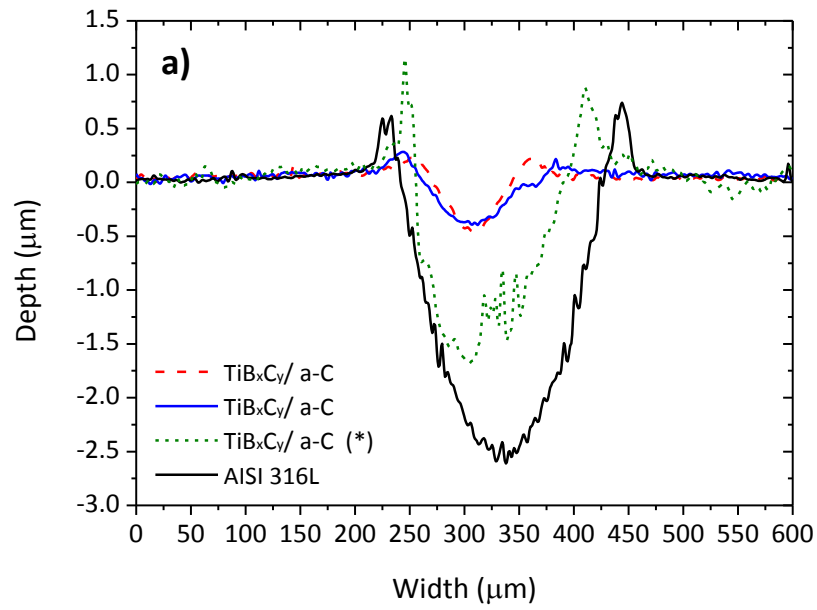


Figure 7